Journal of Materials Research and Technology 29 (2024) 1887–1900

Contents lists available at ScienceDirect

Journal of Materials Research and Technology

journal homepage: www.elsevier.com/locate/jmrt

Tailoring functional properties of a FeMnSi shape memory alloy through thermo-mechanical processing

Mahbod Golrang [a], Maryam Mohri [b,*], Elyas Ghafoori [c], Hesamodin Khodaverdi [a], Mahmoud Nili-Ahmadabadi [a,**]

[a] School of Metallurgy and Materials Engineering, College of Engineering, University of Tehran, Tehran, Iran
[b] Empa, Swiss Federal Laboratories for Materials Science and Technology, Dübendorf 8600, Switzerland
[c] Institute for Steel Construction, Faculty of Civil Engineering and Geodetic Science, Leibniz University Hannover, Hannover 30167, Germany

ARTICLE INFO

Handling Editor: P Rios

Keywords:
FeMnSi shape memory alloys
Shape memory effect
Recovery stress
Pseudoelastic effect

ABSTRACT

The influence of thermo-mechanical processing on the microstructure and functional properties of a Fe–17Mn–5Si–10Cr–4Ni-1(V–C) (wt%) shape memory alloy was systematically investigated. The as-received material was subjected to 25 % cold rolling followed by a recrystallization at 925 °C and single or double aging treatments. Transmission electron microscopy revealed the formation of the ε-martensite and annealing twin boundaries and Shoji-Nishiyama orientation relationships of ε-martensite and γ-austenite in double aged specimen. Cyclic tensile testing demonstrated that the recrystallized and double aged alloy exhibited excellent pseudoelasticity. In the incremental strain test, the alloy achieved the highest peak stress and pseudoelasticity at each cycle. In the constant stresses test, the alloy accumulated a minimal residual strain of only 0.12 % over 50 cycles. This stability was attributed to a strong precipitation strengthening and the interactions between the martensite and the refined microstructural features. In addition, the recrystallized and double aged sample resulted in the greatest recovery stress of 450 MPa upon heating after pre-straining, because of its high yield strength suppressing new martensite formation during cooling process. The results of high-resolution transmission electron microscopy identified a non-Shoji-Nishiyama orientation relationship between the stress-induced ε-martensite after the stress recovery test and γ-austenite matrix, inducing additional irrecoverable strain and raising the recovery stress. Overall, the study can demonstrate that the tailored thermo-mechanical processing enables optimizing the functional performance of FeMnSi alloys.

1. Introduction

Iron-based Shape memory alloys (SMAs) are an important class of smart materials that can recover their original shape after undergoing deformation [1]. Iron-based SMAs have attracted considerable interest due to their low cost [2,3], good workability [4], and excellent mechanical properties [5] compared to traditional NiTi SMAs, exhibiting a wide range of properties in alloys like FeNiMn [6], FeMnSi [7,8], FeNiC [9], FeMnAlNi [10] and FeNiCoTi [11]. Recently, FeMnSi SMAs have attracted particular attention owing to their advantageous low cycle fatigue (LCF) [12–14], high cycle fatigue (HCF) [15–17] and recovery stress [2] properties for civil engineering applications. This unique property results from a reversible, solid-state phase transformation between the γ-austenite with face centered cubic (FCC) structure and ε-martensite with hexagonal close packed (HCP) structure [18]. When heated above the critical temperature they exhibit shape memory effect (SME) [4] and when stress is relieved, they display pseudoelasticity (PE) [12]; in these conditions stress induced ε-martensite reverts back to γ-austenite.

Extensive work has aimed to improve the SME in FeMnSi SMAs through composition modification [19]. It was shown that the stacking fault energy (SFE) from different compositions change the mode of deformation and studies approve that the ε-martensite transformation occurred when the SFE is below 18 mJ/m^2 [20]. Other ways of improving SME are training [21], thermomechanical processing [22,23], severe plastic deformation (SPD) [24], suppressing annealing twins [25], and precipitate optimization [26–29].

The recovery stress generated upon heating constrained specimens to

* Corresponding author.
** Corresponding author.
E-mail addresses: Maryam.Mohri@empa.ch (M. Mohri), Nili@ut.ac.ir (M. Nili-Ahmadabadi).

https://doi.org/10.1016/j.jmrt.2024.01.248
Received 26 December 2023; Received in revised form 22 January 2024; Accepted 27 January 2024
Available online 29 January 2024

reverse transform ε-martensite to γ-austenite evaluates FeMnSi-SMAs potential as prestressing elements in concrete and steel constructions [2,30]. Recovery stress highly depends on activation temperature and prestrain level, with 2–4 % optimal prestrain and 4 % generally sufficient [30]. Approaches to increase FeMnSi-SMA recovery stress include thermomechanical processing [17,18], changing carbon content [31], and optimized aging [32,33]. Yang et al. [34] found 144 h aging at 600 °C (single aging) in solutionized alloy with composition of Fe–17Mn–5Si–10Cr–4Ni-1(V–C) (wt. %) which developed at EMPA, maximized recovery stress (514 MPa) through precipitates enabling high yield strength and substantial transformable martensite. However, such prolonged single aging is impractical for manufacturing. Double aging can accelerate precipitation, as in AA7075 aluminum alloys where first-step clusters provide nuclei for second aging elevated temperature precipitation [35]. Epicier et al. [36] applied double aging to Fe–C–V steel, forming desired carbide size/density in 10 h + 10 days versus 100 days for single aging. Similarly, double aging potentially optimized FeMnSi-SMA precipitates and recovery stress efficiently. A study showed that with double aging the first step at 600 °C for 20 h and second step at 670 °C for 6 h, achieved 509 MPa recovery stress [37].

Recent works have focused on improving the PE of Fe–17Mn–5Si–10Cr–4Ni-1(V–C) (wt.%) SMA to expand the potential applications of FeMnSi alloys, which potentially designed to have high recovery stress [38–42]. Two main sources of movement of Shockley partials dislocations and reversible movements of ε-martensite are possible reasons for the PE during unloading of FeMnSi SMAs [12,14,39]. It was found that grain refinement and optimized heat treatment can significantly enhance the PE of FeMnSi SMAs, attributed to precipitation strain fields [38,39,41]. Aging at 750 °C for 6 h showed the best results on the solution annealed specimens based on experiments analysis [38]. Post-deformation annealing at 925 °C and single-step aging at 750 °C also improved PE substantially [38]. Double aging below 500 °C increased the size of existing precipitates while forming new (C–V–Cr) rich particles with random distribution, further increasing PE [39]. Additive manufacturing methods of directed energy deposition [43] and laser powder bed fusion [40], along with architectured specimen designs [42], have also been applied to improve PE but require cost reductions and be more accessible for civil engineering adoption.

Previous research showed that optimizing PE deteriorates the SME. Although, the total recovery ratio considering both SME and PE is improved [44]. However, the relationships with recovery stress remain unclear. In this work, we further evaluated a Fe-based alloy, subjected to different heat treatments resulting in various PE, under different loading/unloading scenarios for practical assessment. To characterize the functional properties under various conditions, we also subjected samples with different PE to recovery strain and recovery stress measurements. Microstructural analysis was conducted to provide insight into the mechanisms responsible for improved PE in the processed FeMnSi SMAs.

2. Experiments

In this study, an 18 mmØ rebar R18 of Fe–17Mn–5Si–10Cr–4Ni-1 (V–C) (wt.%) was supplied by re-fer AG, Switzerland. The rebar was cast and hot rolled at 1000 °C. Hereinafter, the alloy is named As-received. Subsequently, it was caliber rolled at ambient temperature to a square cross-section with 14.2 mm sides and a strain of 0.25 using a 110 mm roller as shown in Fig. 1 (a). The specimens were recrystallized in vacuum furnace at 925 °C. The Rex-age and Rex-double age specimens respectively were aged under atmospheric condition at 750 °C and additionally 485 °C for 6 h and cooled down to ambient temperature. All the thermomechanical treatments are summarized in Table 1.

The phase fraction and analysis of specimens were identified using a Rigaku X-ray diffractometer with Cu Ka radiation (λ = 0.154 nm) at 45 kV and 200 mA tube current. The examination of the microstructure was conducted using optical microscopy (OM), with a ZEISS Axioskop 2

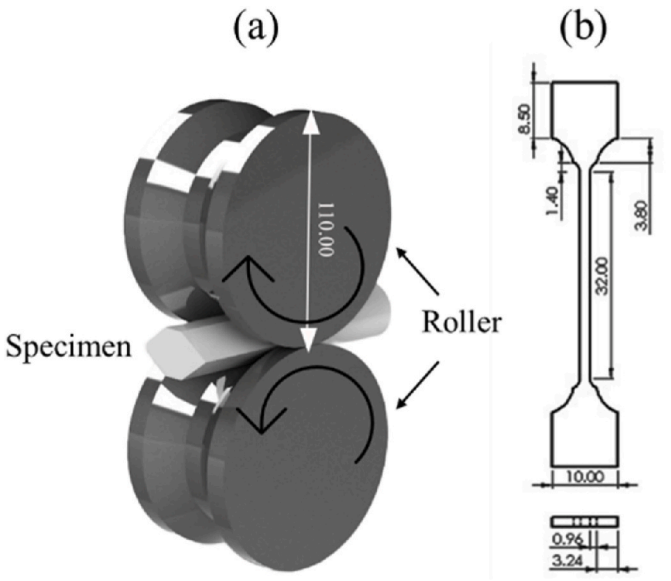

Fig. 1. Schematic representation of (a) caliber roller (b) tensile sample (all dimensions in mm).

Table 1
The summary of the thermomechanical history of the samples.

Sample	Cold rolling	Recrystallizing	Aging
As-received	–	–	–
As-received aged	–	–	750°C-6hr
Rex-aged	0.25	925°C-50 min	750°C-6hr
Rex-double aged	0.25	925°C-50min	750°C-6hr + 485°C-6hr

MAT, as well as field-emission scanning electron microscopy (FESEM) with an FEI Nova NanoSEM 450. Samples for the OM and FESEM observations were polished and etched with a solution of H_2O_2 (35 %), HNO_3 (65 %), and HCl (32 %) (7:30:9). The microstructures are also characterized by high-resolution transmission electron microscopy (HR-TEM; FEI Tecnai F20 series). The HR-TEM specimens are prepared by standard mechanical grinding and electropolishing. The electrolyte was a solution of $HClO_4$ and C_2H_5OH (1:9) at −20 °C and 22 V. For thermal analysis dilatometry was used with Adamel DT1000 to assess the transformation temperatures with 10 mm cylindrical specimens and 2 mm diameter.

The thermomechanical properties of the FeMnSi-SMAs specimens were measured by conducting pre-straining at room temperature while the specimens have austenitic structure and activation experiments. To estimate the stress onset for the martensite transformation, the specimen was loaded to a target strain and fully unloaded, which is known as pre-straining. The details of the tensile test geometry mentioned in Fig. 1 (b). In FeMnSi-SMAs, martensite transformation, plastic flow, or a combination of both causes the nonlinear stress–strain behavior. Previous studies have shown that 0.1 % yield stress as shown in Fig. 2 (a) provides a better estimation for the stress onset for the martensite transformation than the 0.2 % yield stress [45], and thus 0.1 % yield stress was used in this study.

The steps for recovery strain (Fig. 2 (b)) and recovery stress (Fig. 2 (c)) in FeMnSi SMAs during heating can be summarized as follows:

1. Tensile samples were subjected to 4 % load-unload tensile testing with 0.5 mm/min crosshead speed.
2. For recovery strain when heating started, strain began increasing due to thermal expansion until it reached the A_s and then strain

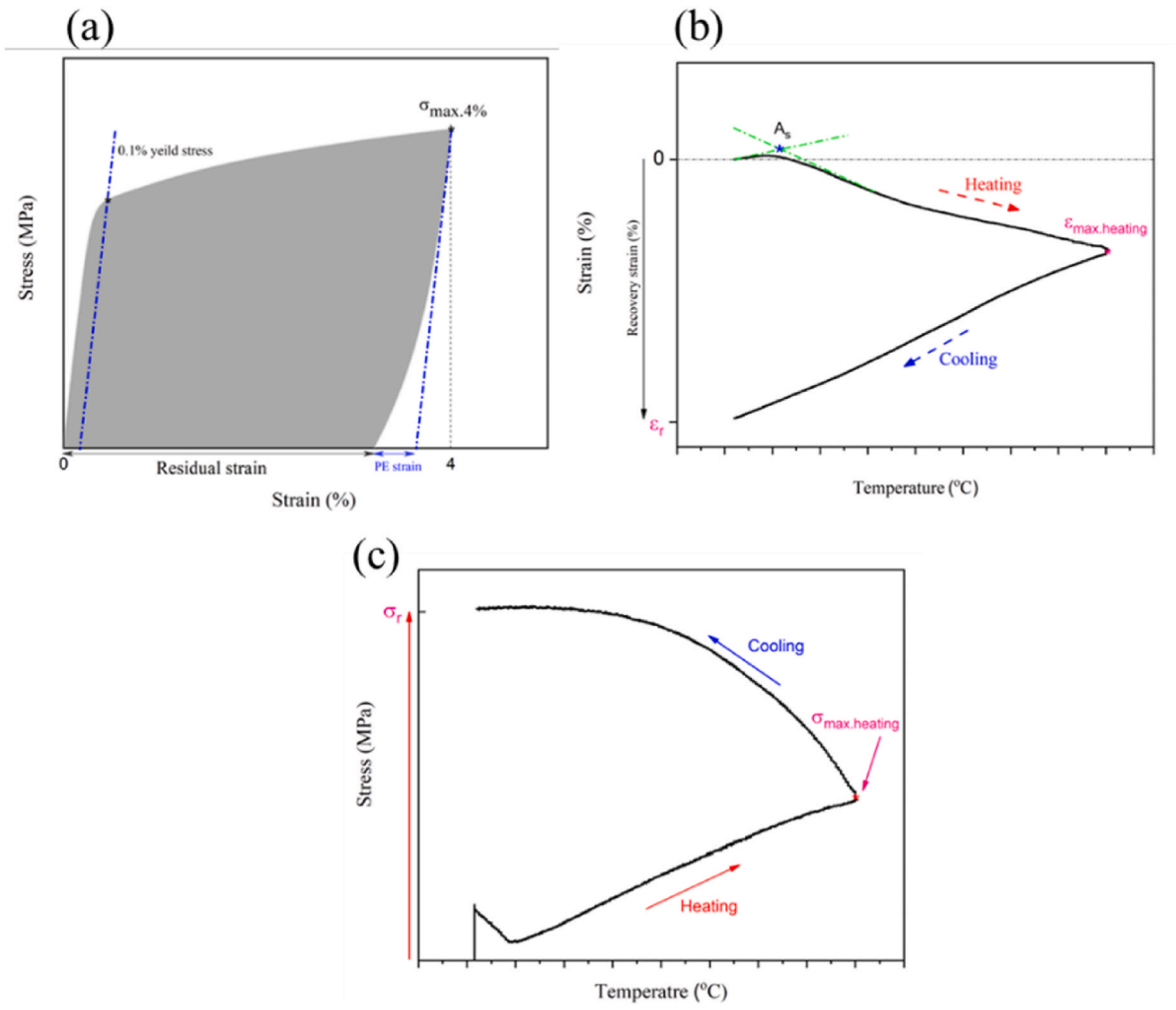

Fig. 2. (a) Typical stress-strain behavior of samples subjected to 4 % load-unload test at room temperature; heating and cooling procedures of (b) recovery strain, (c) recovery stress which started from 23 °C to 180 °C then cooled down to 23 °C under no-constrains and constrains, respectively.

decreasing because of the ε→γ transformation. For the recovery stress tests, the specimens were subjected to a 50 MPa pre-load to prevent buckling resulting from thermal expansion under the lowered stress condition. The initial reduction observed during the first step of the recovery stress test occurs due to the constrained clamping of the specimen combined with its thermal expansion before the A_s, which leads to lowered stress and potential buckling if adequate pre-loading is not applied.

3. Heating continued to reach the maximum temperature T_{max}.
4. Above the A_f temperature, strain increased further from austenite thermal expansion for recovery strain tests. For recovery stress, the change in slope of the stress-temperature curve indicated the A_f.
5. On cooling to room temperature, or recovery strain, significant strain recovery occurred due to thermal contraction until the recovery strain (ε_r) was achieved and reaching the maximum recovery stress (σ_r).

The pre-straining and activation experiments were performed using a Zwick Roell Z020 tensile machine equipped with a climate chamber. Strain was measured using a clip-on extensometer with 0.2 accuracy class per EN ISO 8513. The extensometer directly controlled strain during pre-straining and recovery strain test.

3. Results

3.1. Functional pseudoelastic behavior

The plot in Fig. 3 (a) depicts the cyclic load-unload test with incremental strain up to 10 %. The presence of PE causes the unloading and reloading curves to form hysteresis loops (Fig. 3 (a)) which can dissipate the energy of cyclic loading [4,16,46]. PE calculated according to the non-linearity strain during the unloading as follows:

$$PE\ strain^i = \left(\varepsilon^i_{max} - \varepsilon^i_{unload} - \frac{\sigma^i_{max}}{E_{unload}}\right) \quad (1)$$

$$PE\ (\%) = \frac{PE\ strain^i}{\varepsilon^i_{max} - \varepsilon^i_{initial} - \frac{\sigma^i_{max}}{E_{unload}}} \times 100 \quad (2)$$

PE strain^i is the PE at each cycle of load-unload; $\varepsilon^i_{initial}$ and ε^i_{max} are strain when commence to loading and reached the σ_{max}, respectively. ε^i_{unload} is the strain when the stress reaches zero value.

To increase the PE and decrease the irrecoverable strain in the investigated specimens, several factors were identified. First, it was observed that refining grain size can restrict the movement of the dislocations and generate the back-stress at the tip of the ε-martensite, resulting in improved PE [13,29] as shown in Fig. 6 (g). Microstructural analysis in Fig. 4 (a)-(c) revealed grain refinement from ~14 μm (as-received) to ~5 μm (Rex-double aged) (Fig. 4 (d)–(f)) leading to

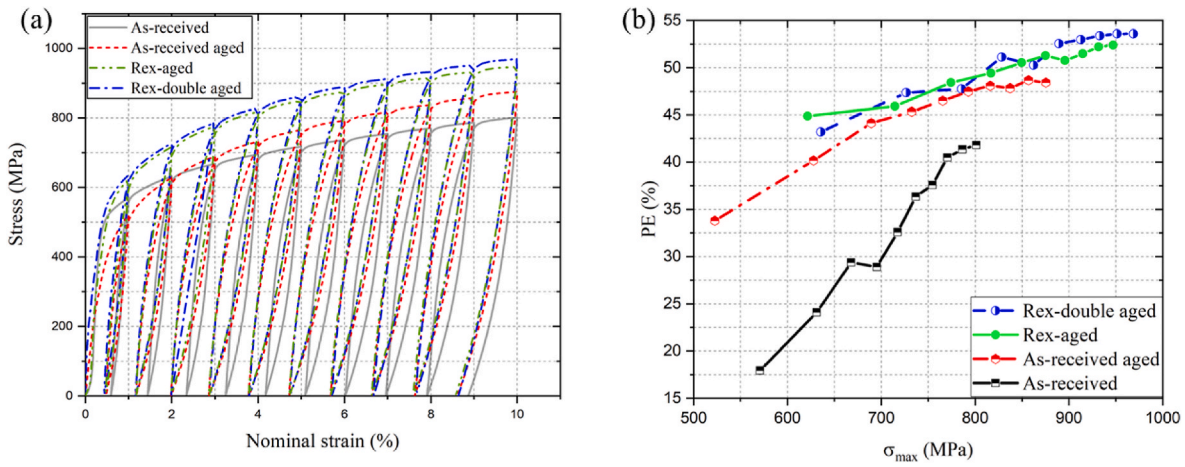

Fig. 3. (a) Cyclic load-unload behavior until 10 % at room temperature, (b) PE - maximum stress at each cycle.

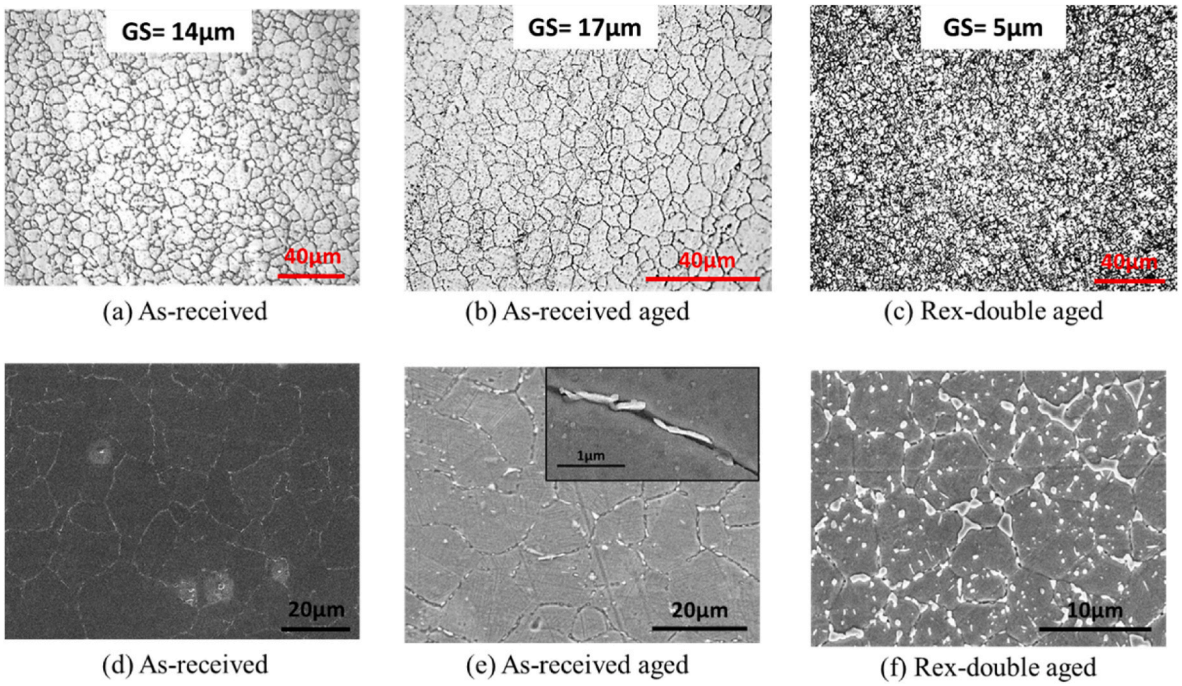

Fig. 4. Representative microstructure by OM (a), (b) and (c); FESEM (d), (e) and (f) where the grain size and precipitation distribution of the As-received (a) and (d), As-received aged (b) and (e), and Rex-double aged (c) and (f) specimens are shown.

~10 % enhancement of PE.

It was found that an increase in stress during loading resulted in a higher formation of ε-martensite and a greater proportion of ε-martensite reverting back to γ-austenite, leading to an increased amount of PE [4]. This finding was consistent when comparing the As-received specimens with the rest of the samples. Fig. 3 (b) illustrates the relationship between PE and the maximum stress at each cycle. It is evident that an increase in σ_{max} led to an improvement in PE, with PE values increasing from approximately 33 %–45 % in the As-received aged and approximately 43 %–53 % in the Rex-double aged specimens.

Finally, the reduction in nucleation barrier energy of the ε-martensite can improve PE by (1) increasing the density of post-annealing SFs [39,47]; and (2) introducing precipitates (VC particles in this study) that impose a strain field around semi-coherent particles [37,47–50]. In Rex-double aged (Fig. 4(f)–. 6 (e)–(f)) increasing precipitates with more random distribution as compared to As-received aged, induced the strain field around the particles which is considered to be effective for PE improvement.

Fig. 5 illustrates the cyclic load-unload test conducted on specimens subjected to a tensile stress of 500 MPa, followed by unloading. This procedure was repeated 50 times for each sample. According to the figure, the initial cycle displayed a higher irrecoverable strain, which is influenced by the PE and the 0.1 % yield stress of individual alloy.

For the As-received and As-received aged specimens (Fig. 5 (a), (b)), while the Young's modulus ($E_{loading}$) remained approximately constant, the yield stress decreased from 300 MPa in the As-received state to 200 MPa in the As-received aged state. Consequently, these reductions led to a decrease in the irrecoverable strain from 0.84 % to 0.66 %. Moreover, it was observed that the PE of the As-received aged specimens significantly improved compared to the As-received specimen.

For the recrystallized and aged specimens (Fig. 5 (c), (d)), $E_{loading}$ decreased while yield stress increased compared to the As-received condition. The Rex-aged specimen showed 0.07 % irrecoverable strain in the first cycle, but this increased to 0.12 % for the Rex-double aged

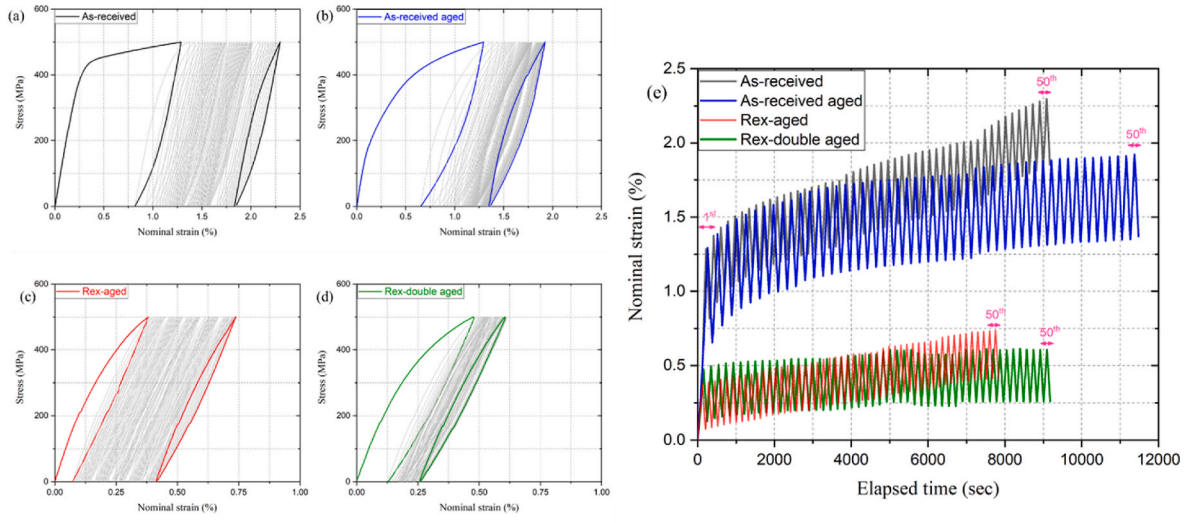

Fig. 5. Cyclic load-unload test at room temperature between constant stresses of zero and 500 MPa for As-received (a), As-received aged (b), Rex-aged (c), Rex-double aged (d). (e) Nominal strain-elapsed time curves for different samples.

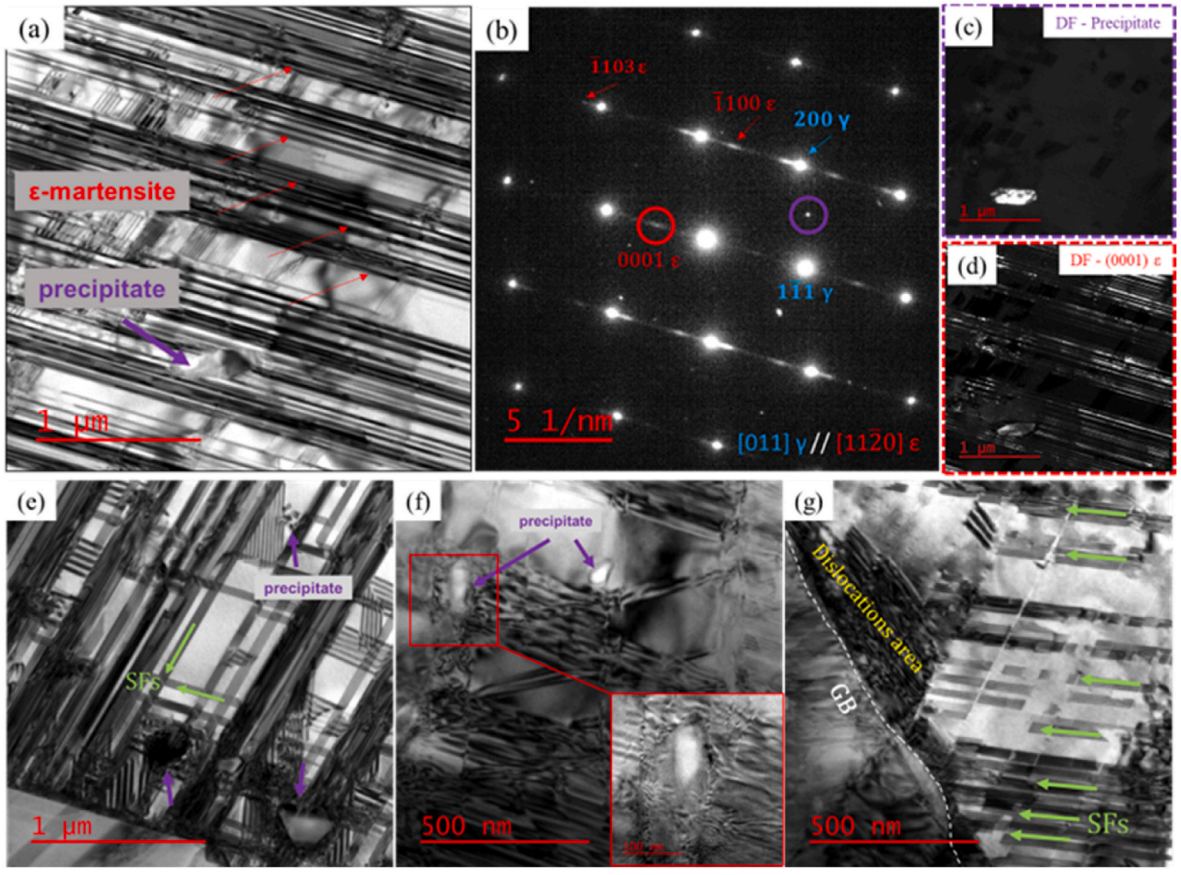

Fig. 6. (a) BF TEM image of the Rex-double aged specimen after the 2 % load-unload test. (b) Indexed SADP which approved the S–N orientation relationship with $[011]_\gamma$ and $[11\ \bar{2}\ 0]_\varepsilon$ zone axis. DF TEM image of a precipitate (c) and (d) $(0001)_\varepsilon$ planes which were parallel to $(1\ \bar{1}\ 1)_\gamma$. BF TEM images in (e), (f) show the complex interaction of SFs (green arrows) and ε-martensite with the precipitates (purple arrows) and (g) reveals the formation of paralleled SFs of Rex-double aged. (For interpretation of the references to colour in this figure legend, the reader is referred to the Web version of this article.)

sample. The lower yield stress in the double aged specimen resulted in more ε-martensite formation. Prior studies indicate that new particles formed during second aging provide increased nucleation sites for ε-martensite and stacking faults in subsequent cycles.

The PE was calculated and is listed in Table 2. The highest PE of 41.6 % occurred in the Rex-aged specimen for the initial cycle, increasing to 91.28 % after 50 cycles and the Rex-double aged PE increased significantly from 40 % to 99.42 %, maintaining stable PE behavior throughout cycling.

Fig. 5 (e) presents the strain-time curves obtained for the different

Table 2
PE strain of the cyclic load-unload test and cumulative residual strain (CRS) of Fig. 5.

		As-received	As-received aged	Rex-aged	Rex-double aged
PE (%)	1st	16.32	31.83	41.6	40
	50th	76.47	93.07	91.28	99.42
Cumulative Residual Strain (CRS) (%)		1.03	0.71	0.33	0.12

specimen types during load-unload testing. These curves exhibit cumulative residual strain for each sample - referred to as CRS - which is quantified in Table 2. As observed in the stress-strain curves (Fig. 5 (a)–(d)), an accumulative residual strain remained upon unloading to zero MPa over the multiple cycles. The highest CRS of 1.03 % occurred in the As-received specimen, while the Rex-double aged sample displayed the lowest CRS of 0.12 %. In addition, the figure shows almost a constant nominal strain for Rex-double aged, while in the other specimens it increases with increasing load-unload cycles. The former specimen stability is due to its higher yield strength and improved PE.

3.2. Microstructure changes in recovery strain

Fig. 6 (a), shows a bright-field (BF) TEM image of Rex-double aged after 2 % load-unload test contains a structure with parallel ε-martensite laths and a precipitate which was shown in dark-filed (DF) TEM image of Fig. 6 (c). Besides, the parallel SFs (Fig. 6 (g)) are theorized to further facilitate the γ↔ε martensitic transformation by lowering the chance for ε-martensite lathes to collide with one another. This collision could otherwise lead to the development of α′-martensite in the SFs intersection during tensile loading and unloading tests which eventually makes difficult γ↔ε transformation [22,25,29].

In the selective area diffraction pattern (SADP) shown in Fig. 6 (b), streaks are observed that correspond to the ε-martensite phase, as confirmed by the DF TEM image in Fig. 6 (d). The streaking arises due to the planar nature and crystallographic defects associated with the thin

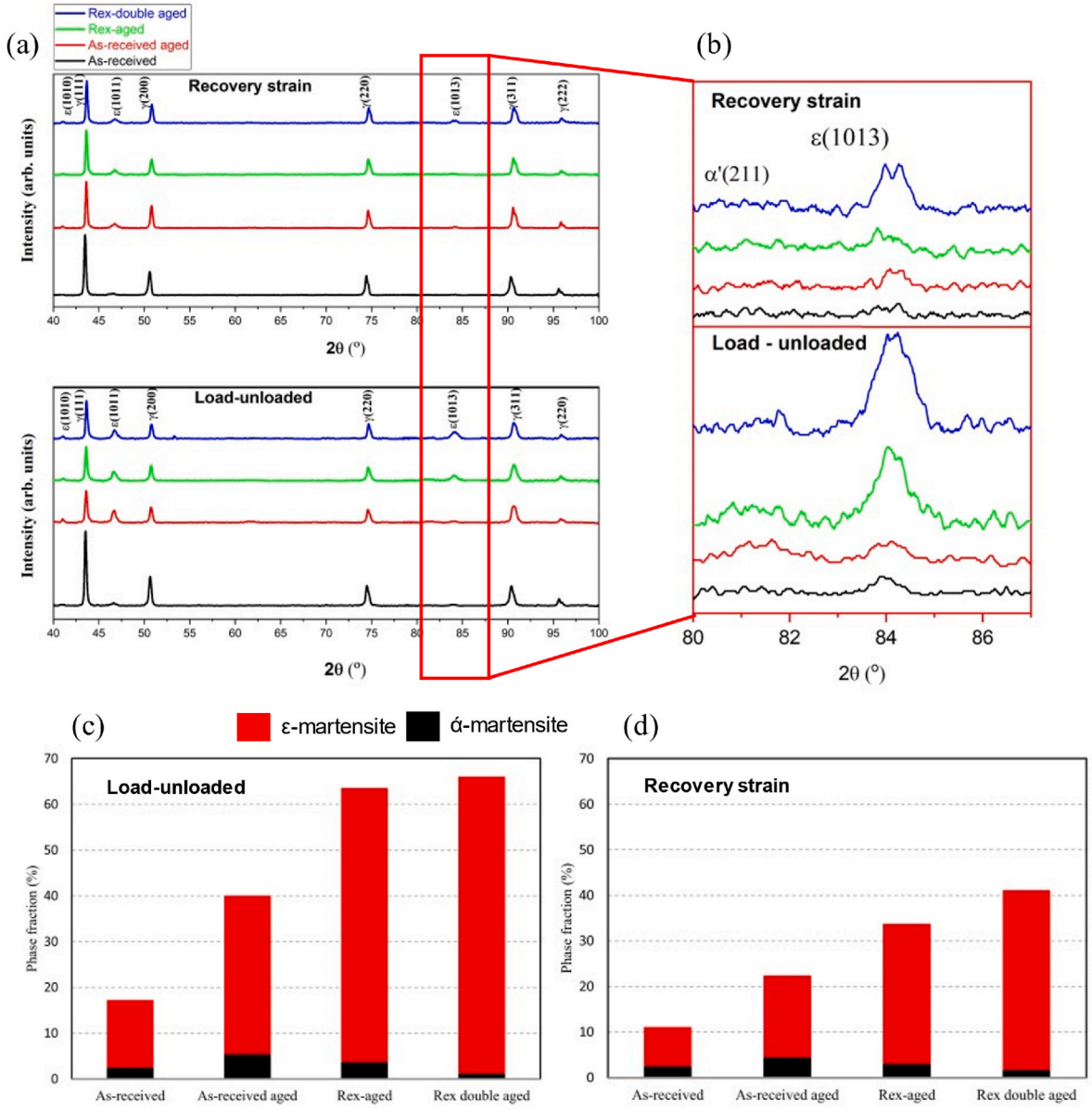

Fig. 7. (a) XRD pattern of the specimens after 4 % load-unload and recovery strain at 200 °C for 30 min; (b) higher magnification of 80° - 90° (c) Phase fractions after the load-unload (d) and after the recovery strain.

plates of ε-martensite. Analysis of the SADP and DF TEM data indicate that the orientation relationship between the ε-martensite and austenitic matrix follows the Shoji-Nishiyama (S–N) relationship [51]. This assignment is based on the alignment of the streaks along <111> directions in the SADP, consistent with Shoji-Nishiyama arrangement where {111} planes in austenite are parallel to {0001} planes in ε-martensite. The presence of planar defects causes spot broadening perpendicular to the planes, resulting in streaking along <111> directions in the SADP. Fig. 7 (a) represents the X-ray diffraction patterns of the specimens after 4 % load-unload and recovery strained at 200 °C for 30 min. The higher magnification of the 80–90° of 2 theta superimposed in Fig. 7 (b) which shows the weak peak of ά-martensite at 81.5° and a peak at 84°. The plane spacing of the (1013) according to Bragg's law is calculated 1.15 A^o which is compatible with the streak belonging to the {10.3} in SADP. Based on TEM images, confirm that the peak at 84° is corresponds to (1013) plane of ε-martensite. This plane also has seen in the XRD pattern of the heat-treated and additively manufactured FeMnSi SMAs [40] which is activated after the loading and unloading in this study. Jee et al. [52], shows that the (1013) responsible for the largest expansion and the contraction during the forward martensite transformation with c/a is almost $(8/3)^{1/2}$.

The method in Ref. [53] was used to calculate the volume fractions of ά-martensite and ε-martensite, and Fig. 7 (c), (d) show the results of the specimens after load-unload and strain recovered at 200 °C for 30 min, respectively. Fig. 7 (c) shows an upward trend ε-martensite formation while we have the lowest portion of the ά-martensite in Rex-double aged specimen. The highest fraction of the ά-martensite is in the As-received sample due the incoherency of the precipitations and possible intersection of multi-variant ε-martensite while in Rex-double aged sample due to the lower possibility of the plastic deformation and the formation of the single variant martensite, lowest portion of ά-martensite seen after unloading.

The results of the analysis after loading and unloading are in agreement with the previous findings [38,39]. The α' and ε-martensite phases formed in the specimens before the load-unload due to the difference in thermal expansion coefficients between the matrix and precipitates during post-aging cool down. According to previous study [39], The highest ε-martensite fraction was observed in the Rex-aged sample before subjecting to 4 % strain, while the Rex-double aged sample showed the highest ε-martensite fraction after load-unload. TEM images revealed that although the ε-martensite fraction in Rex-double aged was lower than in Rex-aged, precipitate coherency substantially improved and ε-martensite variant selection became more limited in the double aged sample [39]. Overall, the increased precipitate density provided more nucleation sites for ε-martensite formation, leading to a higher retained ε-martensite fraction in the Rex-double aged condition after load-unload. Meanwhile, the reduced ε-martensite variant diversity decreased α'-martensite formation due to limited intersection of ε variants.

After the recovery strain process, the α'-martensite phase fraction remained mostly unchanged. However, the ε-martensite transformed substantially back to austenite, decreasing from ~65 % to ~41 % in the Rex-double aged specimen (~24 % reduction). The largest reduction in ε-martensite fraction was observed in the Rex-aged specimens at approximately 30 %, while the As-received condition showed the lowest reduction of ~6 %.

The ε-martensitic transformation in FeMnSi SMAs involves the movement of $1/6 < 11\bar{2} >$ Shockley partial dislocations along alter-

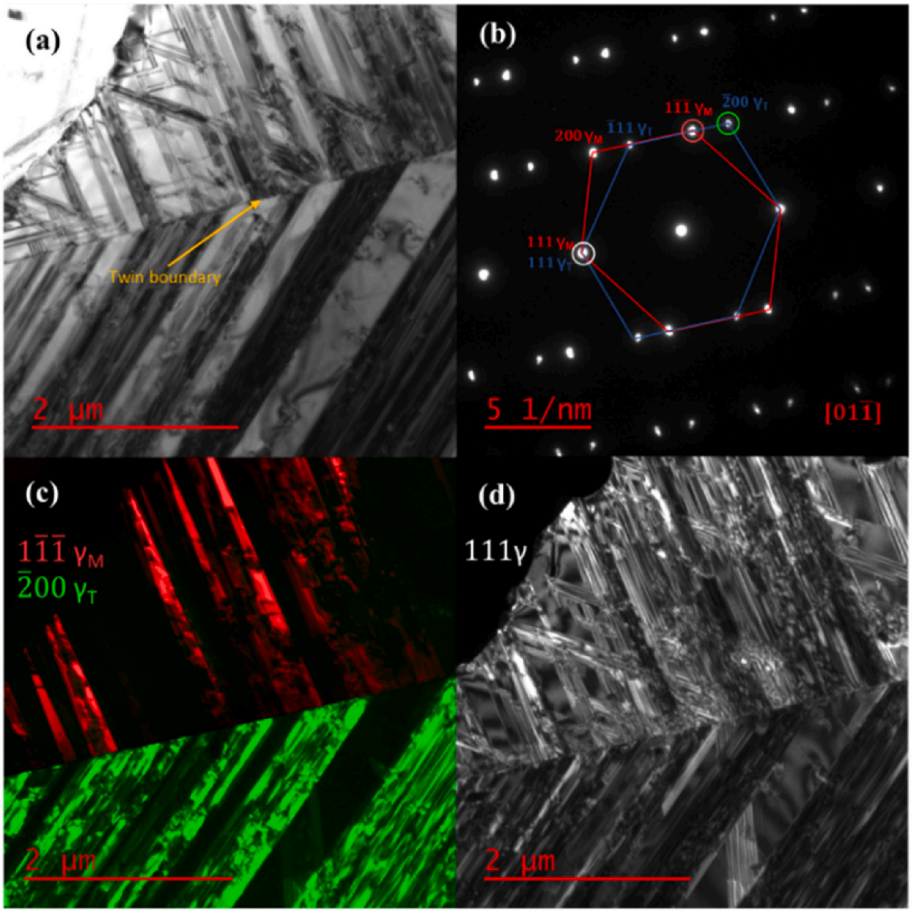

Fig. 8. (a) BF TEM image of the Rex double aged specimen after 2 % load-unload testing, revealing a large twin. (b) SADP confirms twin formation with respect to [01 $\bar{1}$] zone axis. (c–d) DF TEM images demonstrate differing orientations between the twinned regions.

nating {111} planes of the austenite FCC structure. In contrast, the $\{111\}\langle 11\overline{2} >$ twinning mechanism occurs through movement of $1/6 < 11\overline{2} >$ Shockley partials along consecutive {111} planes. Formation of annealing twins via conventional thermomechanical processing of FeMnSi SMAs has been previously reported [25,50]. In this work, Fig. 8 shows a large twin boundary (TB) present in the Rex-double aged specimen after load-unload test. Numerous parallel twin plates and ε-martensite laths are observed.

Recovery strain tests were conducted by initially straining the specimens to 4 % at room temperature (Fig. 9 (a)) followed by heating to 180 °C then cooling back down, in order to assess the SME. The measured recovery strain as a function of temperature is plotted in Fig. 9 (b) for the different samples. Four distinct stages occurred in the strain-temperature curves during the thermal cycle. First, strain increased due to thermal expansion as the temperature rose from ambient, with a 57 °C A_s measured for the As-received aged sample, slightly higher than the Rex-aged specimen. Second, upon heating above A_s, strain decreased as the ε→γ reverse transformation began, continuing until the A_f temperature was reached; in this test, only the Rex-aged and As-received aged samples achieved A_f, while the Rex-double aged did not, likely contributing to its poorer shape memory response. Third, above A_f the transformation completed and strain then increased again due to further thermal expansion of the fully austenitic microstructure, clearly observed for the Rex-aged and As-received aged conditions. Finally, during cooling, strain decreased due to thermal contraction. The Rex-double aged sample exhibited the lowest shape recovery at ~0.45 %, while the As-received aged showed the highest at ~0.78 %.

Fig. 10 shows the shape recovery of different specimens (black columns), the shape recovery percentage calculated according to the shape recovery strain from Fig. 9 (a, c) according to Eq (3):

$$shape\ recovery = \frac{recovery\ strain}{residual\ strain} \times 100 \quad (3)$$

Recovery strain derived from the absolute values of nominal strain in Fig. 9 (b) and residual strain derived from Fig. 9 (a). The highest shape recovery achieved in As-received aged with ~25 % and the Rex-double aged sample showed only ~17 % recovery, far lower than the As-received aged and Rex-aged samples. The red columns in Fig. 10 represents the difference between the ε-martensite phase fraction in Fig. 7-c and Fig. 7-d. By contraction of the ε-martensite fractions of prior and after recovery ε-martensite at 200 °C for 30 min approved that highest amount of the ε→γ transformed in Rex-aged and Rex-double aged samples with ~30 % and ~25 % of ε-martensite transformed to austenite after recovery at higher temperature, respectively. It is evident that one reason for the weak recovery strain response of the Rex-double aged sample (Fig. 9(b)) is related to its high A_f temperature, resulting in a considerable portion of the ε-martensite remaining untransformed. Dilatometry test results showed that the A_f temperatures of the As-received and Rex-double aged alloys were 189 and 185 °C, respectively, as presented in the appendix a. In addition, it appears that the

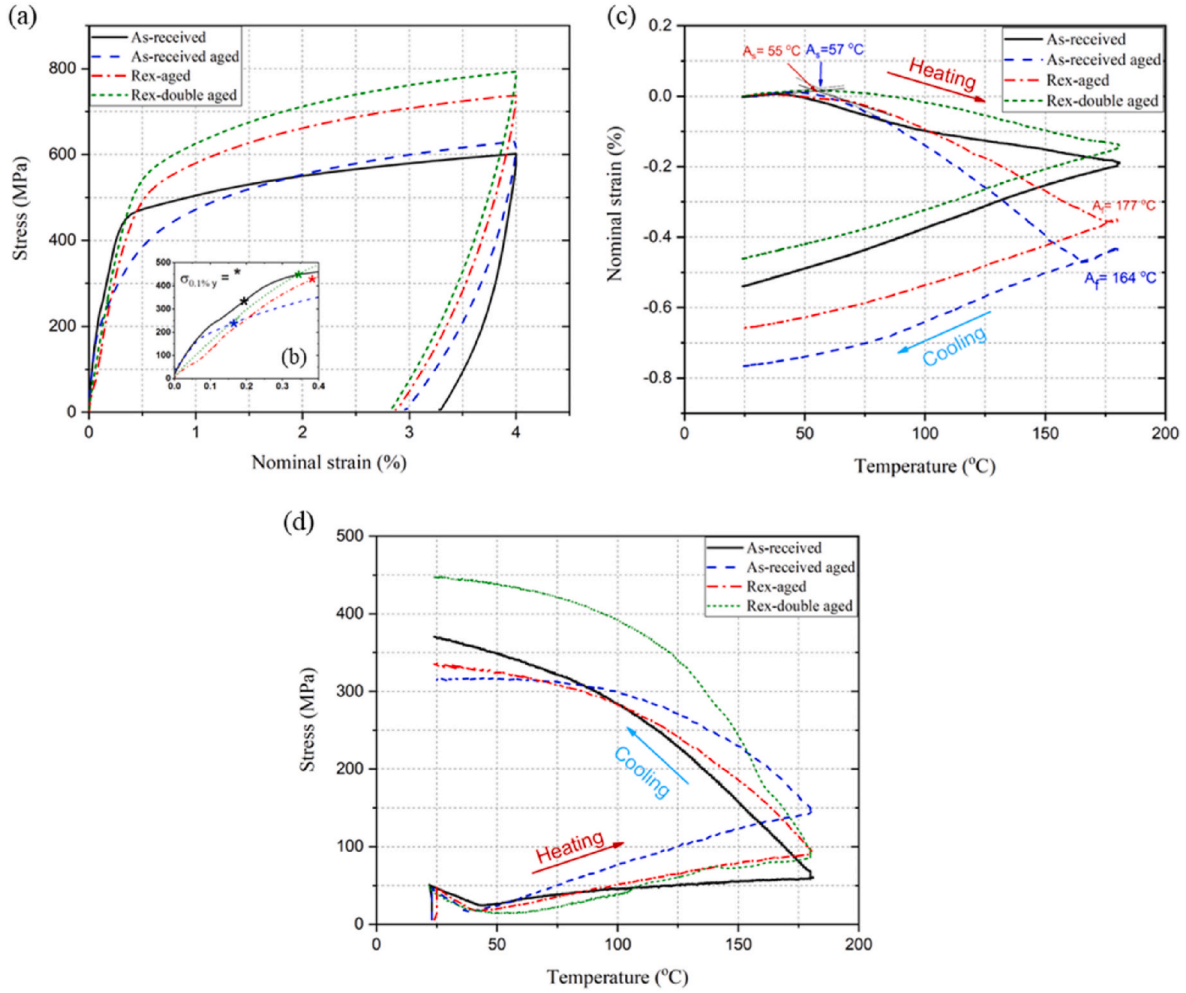

Fig. 9. (a) 4 % pre-straining of the specimens at room temperature, (b) higher magnification of the tensile test which shows the 0.1 % yield stress with *. (c) Recovery strain with maximum heating temperature of 180 °C after subjecting the specimens to 4 % load-unload test. (d) Recovery stress-temperature diagram with maximum heating temperature of 180 °C after subjecting the specimens to 4 % load-unload test.

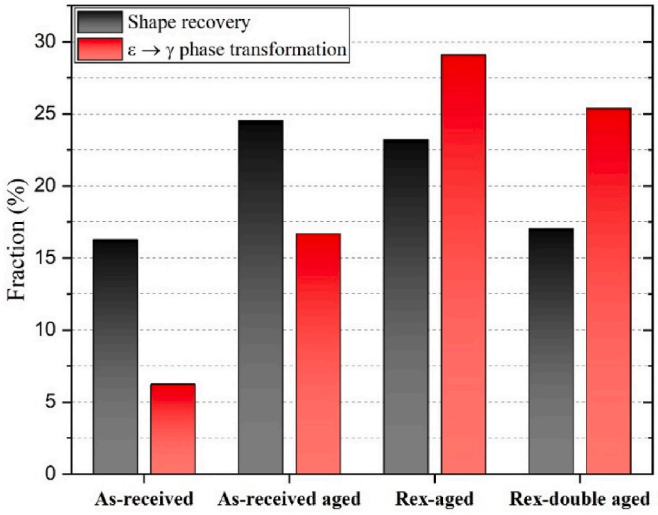

Fig. 10. Shape recovery derived from recovery strain test data and calculated by Eq (3) (black columns); ε→γ phase transformation fractions from ε-martensite to γ-austenite calculated based on ε-martensite percentages post-loading/unloading and recovery strain assessments per Fig. 3 (red columns). (For interpretation of the references to colour in this figure legend, the reader is referred to the Web version of this article.)

enhancement of PE can deteriorate the shape recovery properties [44]. This deterioration is due to limitations in the transformation from ε-martensite to γ-austenite. Primarily, the reverse transformation occurs during the unloading process. Despite the highest reversion in recrystallized and aged specimens at 200 °C, the remained fraction of the ε-martensite is still too high, this will be discussed in section 4.2.

3.3. Recovery stress formation in FeMnSi

Fig. 9 (a) shows the stress-strain curves obtained by pre-straining the samples to 4 % for recovery stress measurements and in Fig. 9 (d) recovery stress-temperature curves are illustrated. The As-received aged sample exhibited the weakest recovery stress response, with value below 350 MPa This weak response is attributed to the enhancement of the PE by means of precipitation in the As-received aged specimen enabling easy stress-induced martensite formation to accommodate the stress during cooling. However, the Rex-double aged sample displayed the highest recovery stress of approximately 450 MPa.

The maximum stress at 180 °C, denoted as $\sigma_{max.180}$, is found to be highest in the As-received aged specimen. The $\sigma_{max.180}$ is lowest in the As-received sample, while the Rex-aged and Rex-double aged samples showed approximately the same stress value. However, despite having the highest $\sigma_{max.180}$, the As-received aged sample displays the lowest recovery stress at room temperature (referred to as σ_r). Previous studies have shown that improving the recovery strain does not necessarily improve recovery stress behavior [31,50], as evidenced by the As-received aged sample exhibiting the highest σ_{max} at 180 °C due to the ε→γ transformation, yet the lowest σ_r due to its low 0.1 % yield stress. In contrast, the Rex-double aged specimen showed the highest σ_r of 450 MPa, resulting from its elevated 0.1 % yield stress coupled with sufficient ε→γ transformation. To understand the reason behind the high recovery stress obtained for the Rex-double aged specimen, TEM microstructural analysis was performed.

Fig. 11 (a) shows BF TEM image of the Rex-double aged specimen

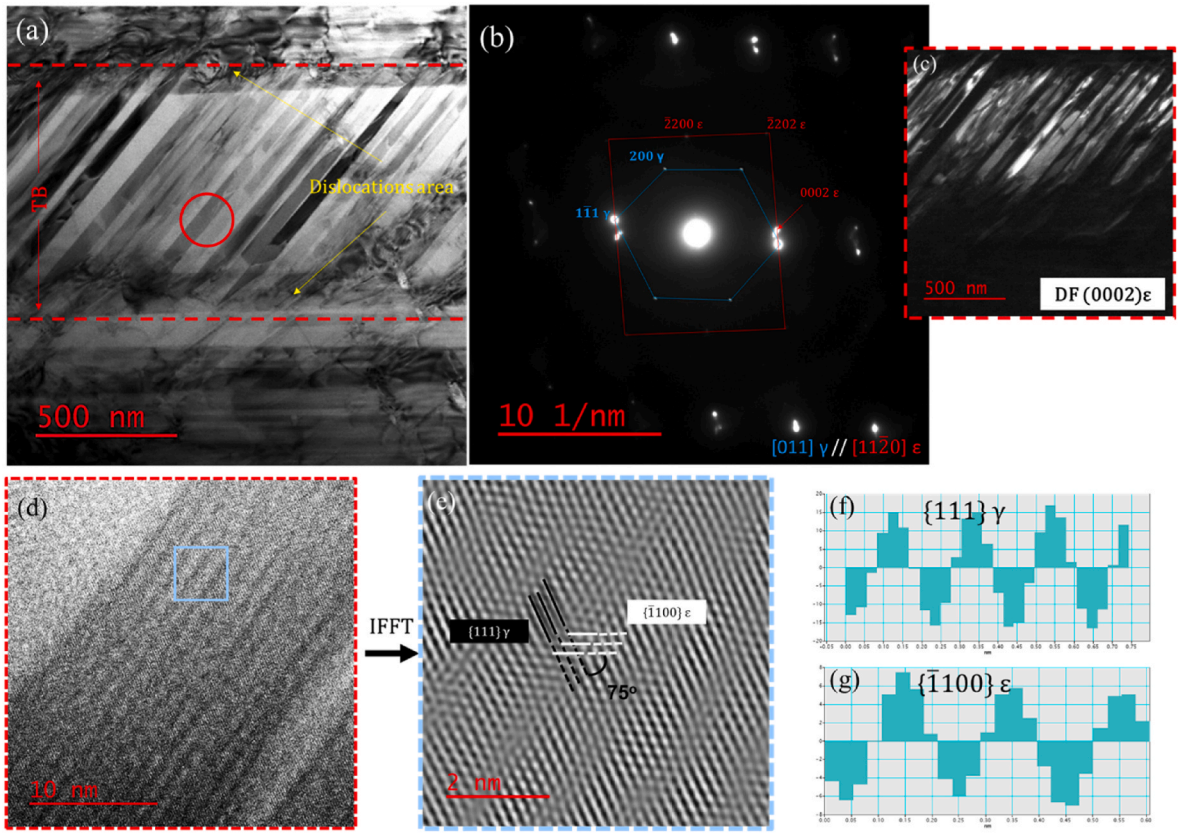

Fig. 11. (a) BF TEM image showing TB and parallel ε-martensite laths inside the TB after recovery stress testing. (b) SADP of the red circle in (a); (c) DF TEM image of the (0002) ε plane. (d) High-resolution (HR) BF TEM of the red circled area in (a) revealing thin ε-martensite laths. (e) Inverse fast Fourier transform (IFFT) of (d) with inter-fringe spacing measurements of (f) {111} γ and (g) {$\bar{1}$1 00} ε planes. (For interpretation of the references to colour in this figure legend, the reader is referred to the Web version of this article.)

after recovery stress testing. The TEM image shows a large twin covered by dislocations and extensive parallel lines. The formation of non-S-N orientation ε-martensite in this specimen is evident in the SADP in Fig. 11 (b), showing a misorientation relative to the $(1\ \bar{1}\ 1)\gamma$ and $(0002)\varepsilon$ planes. Fig. 11 (c) shows a DF TEM image of the $(0002)\varepsilon$ plane, demonstrating ε-martensite laths formation inside the TBs with wedge-shape boundaries. Peng et al. [25] revealed that interactions between pre-existing twin and stress-induced ε-martensite can substantially distort TBs, causing them to produce the uneven TBs. Fig. 11 (d) shows an atomic resolution magnification of the area circled in red in Fig. 11 (a). An inverse fast Fourier transform (IFFT) of this region is presented in Fig. 11 (e), revealing clear atomic layers in the magnified section. Lattice fringe measurements on the matrix in Fig. 11 (f) indicate an average spacing of 2.09 nm, corresponding to the $(111)\gamma$ plane marked by black lines in Fig. 11 (f). Fig. 11 (g) indicates a lattice fringe spacing of ~2.19 nm for the $\{\bar{1}1\ 00\}$ ε planes of the ε-martensite, marked by white parallel lines in Fig. 11 (f). In Fig. 11 (e), the observed misorientation angle between the $(1\ \bar{1}\ 1)\gamma$ matrix and $(\bar{2}2\ 00)$ ε-martensite was approximately 75°, which agrees well with the SADP analysis in Fig. 11 (b). However, according to the S–N orientation relationship, the misorientation between these two planes should be approximately 60°, as presented in Fig. 6.

The atomic resolution imaging and diffraction analyses indicate stress-induced transformation of the austenite matrix to elongated ε-martensite variants during recovery stress testing. While according to previous works [22,39] and Fig. 6, the S–N orientation relationship is the dominant orientation relationship between γ and ε-martensite.

4. Discussion

4.1. The pseudoelasticity and annealing twins

Thick annealing twins formed in the specimens after thermo-mechanical processing, prior to tensile testing [38,39]. During tensile pre-straining, the pile-up of the SFs [54] and dislocations [55] at the TBs increase the TBs' energy and provide preferential sites for nucleation of new internal twins and ε-martensite variants. Hung et al. [56] reported that in TWIP steel, nano twins can readily nucleate at annealing TBs when dislocations concentrate at those annealing TBs. In this study, numerous nanoscale parallel twins and thin ε-martensite laths were observed to have nucleated at the TBs of the pre-existing annealing twins, as shown in Fig. 8 (a). The obstacles provided by modified grain size, more annealing twins and precipitates result in increased ε-martensite formation to 65 %, as evidenced by the phase fraction measurements in Fig. 7 (c). The functional cyclic load-unload tests demonstrated enhanced PE in both incremental strain and constant stress modes, as depicted in Figs. 3 and 5, respectively. The low CRS and minor improvement in PE for the Rex-double aged specimen indicates stable PE behavior during cyclic testing.

4.2. The annealing twins' effect on the recovery strain and recovery stress

Since Kajiwara [26] found NbC precipitates can improve SME in FeMnSi alloys, many studies have investigated the influence of different carbide and nitride compositions (e.g. $Cr_{23}C_6$ [28], VN [27], VC [57]) and particle size ranges. For instance, NbC larger than 50 nm enhanced SME by providing additional nucleation sites and higher ε-martensite fractions [58]. However, Lai et al. [29] showed extremely fine 6 nm VC particles formed during low temperature 650 °C aging did not improve SME, while 21 nm VC from aging above 700 °C did increase it. Based on this, the As-received aged sample with 20 nm [39] V-rich precipitates was expected to exhibit good SME and it has the highest recovery strain according to Fig. 9 (c). The Rex-aged sample, with similar precipitation condition (both aged at 750 °C for 6 h) but different spatial distribution and shapes, was believed to potentially show even better recovery strain response compared to As-received aged, but did not. Most unexpectedly, the Rex-double aged sample with pre-existing particles grown to ~90 nm [39] and increased precipitate density showed the lowest SME, despite the precipitation condition being similar to prior work where carbides/nitrides effectively improved shape memory behavior. The deterioration of SME for Rex-double aged appears to arise from factors beyond just particle size and distribution in this alloy.

Peng et al. [59] reported that coarse-grained FeMnSi SMAs exhibit giant SME compared to finer-grained alloys for two reasons. First, they stated that increasing grain size promotes more stress-induced ε-martensite by suppressing grain boundary effects. However, in this study, higher ε-martensite volume fractions were observed in the Rex-double aged and Rex-aged samples, which have a finer average grain size of ~4 μm compared to the As-received and As-received aged conditions with a coarser ~15 μm grain size (Fig. 4). Second, they claimed larger grains increase single-variant ε-martensite formation, reducing inter-variant intersections. But here, the finer recrystallized grains showed lower α'-martensite fractions compared to the coarser As-received and As-received aged samples (Fig. 7). Therefore, the results of this work contradict with previous findings, as enhanced martensitic transformation and reversibility were exhibited in the finer-grained recrystallized and aged samples, despite improved shape memory properties in coarse-grained FeMnSi SMAs.

The presence of large annealing twins has been found to negatively impact shape memory behavior, as reported by Wen et al. [25], showed that in Fe-20.2Mn-5.6Si-8.9Cr-5.0Ni SMA (wt.%) increasing TB density leads to greater interaction between stress-induced ε-martensite formed during pre-straining and the annealing twins, which hinders reversible martensitic transformation and lowers SME. Fig. 7 (c) and (d) show the phase fractions before and after the recovery strain process. After recovery strain, the Rex-double aged sample retained the highest fraction of ε-martensite. This confirms that despite undergoing substantial ε→γ transformation after pseudoelastic load-unload test and shape recovery process, a higher residual ε-martensite fraction remained in the Rex-double aged microstructure. The incomplete reverse transformation contributed to the reduced SME exhibited by this condition. The likelihood of forming annealing twins is inversely related to SFE where recovery strain increased with higher SFE in Fe–Mn–Si alloys [60,61]. However, the SFE must remain below a critical value for stress-induced ε-martensite to be the preferred deformation mode. The calculated SFE for the FeMnSi SMAs studied here is 5.72 mJ/m^2 [38]. This shows that despite the formation of precipitates with sufficient size and lower ά-martensite phase fraction after load-unload (Fig. 7 (c), (d)), the annealing TBs (which increase with decreasing grain size [24,62]) deteriorate the SME in these FeMnSi-SMAs. Recent study shows that improving the PE can deteriorate the SME to some extent by limiting the ε-martensite after unloading [44]. Luo et al. [62] investigated the effect of the ε-martensite phase fractions to the SME prior to straining in a bending test and found that a lower ε-martensite phase fraction with proper thermomechanical treatment or training condition and larger grain size, would result in higher recovery strain behavior. This matter to some extent shows consistency with the As-received aged and Rex-double aged behavior in this study.

For recovery stress, improving recovery strain does not necessarily also improve the recovery stress response at room temperature [31]. Recovery stress is primarily influenced by two key factors - the yielding behavior and the precipitate characteristics in the alloy. Yielding in FeMnSi SMAs involves complex interactions between normal dislocation slip and the martensitic γ→ε phase transformation [63]. This transformation occurs through the motion of perfect dislocations as well as Shockley partial dislocations on the close-packed {111} planes of the FCC austenite structure [63]. It can also occur by the formation of stacking faults on alternative {111} plane, which creates the hexagonal stacking sequence of the epsilon martensite structure. Therefore, the 0.1 % yield point commonly reported represents a combination of normal dislocation plasticity and stress-induced epsilon martensitic

transformation occurring together in these alloys.

A higher yield stress indicates greater resistance to the motion of perfect dislocations as well as more difficult slip of the Shockley partial dislocations required for the martensitic transformation. Furthermore, Wang et al. [33] found that new stress-induced epsilon martensite forms during cooling after pre-straining, and this new martensite has different characteristics compared to the prior martensite variants formed during loading. This result demonstrates that when the yield stress is sufficiently high after pre-straining, it can prevent further martensitic transformation from occurring during the subsequent cool down. This effect is evidenced by the Rex-double aged sample exhibiting the highest 0.1 % yield point in Fig. 9 (b), which restricts additional martensite formation during cool down following pre-straining since the high strength resists the slip of partial dislocations required for transformation.

The VC-rich particles present in the microstructure influence the yield stress through primary mechanisms. The particles can hinder the motion of perfect dislocations via Orowan strengthening [64], as described by the Ashby-Orowan equation relating particle spacing and strength [65]. This effect of VC particles explains the weak recovery stress exhibited by the As-received aged sample compared to the Rex-double aged condition. The diameter and distribution of the particles are two important parameters that increase the yield stress according to the Ashby-Orowan equation [65]. In the As-received aged sample, precipitation mostly occurred along grain boundaries (Fig. 4 (b), (e)), while in the Rex-double aged sample, the particles were distributed more randomly (Fig. 4 (c), (f)). Additionally, in the Rex-double aged sample, the size of the primary precipitates increased from 15-30 nm to 70–115 nm after the second aging treatment at 485 °C for 6 h [39].

Additionally, HR-TEM analysis revealed a non-S-N orientation relationship between the ε-martensite and austenite matrix inside the annealing twins which surrounded by dislocation areas, as shown in Fig. 11. This differs from the dominant S–N relationship observed after load-unload testing in Fig. 6. Recently, Baik et al. [66] found that in an Fe–15Mn–2Cr-0.6C-0.06 N (wt.%) alloy, as strain increased, secondary twins and ε-martensite variants formed that did not have the S–N orientation relationship. These developed by intersection of two primary twin or ε-martensite bands. This non-S-N orientation relationship arises in the Rex-double aged sample due to the complex shear and strain conditions induced during recovery stress testing, which differs from conventional tension. The change in transformation orientation results in additional irrecoverable strain, contributing to the high recovery stress response.

The schematic in Fig. 12 illustrates the microstructural evolution during loading and subsequent recovery. Initially, the thermally induced ε-martensite and annealing TBs are present. At peak loading, stress-induced ε-martensite forms within the austenite matrix and TBs. Numerous dislocations are also generated, concentrated around the TBs. During unloading, some of the stress-induced martensite reverses through partial dislocation slip, but ε-martensite largely remains within the TBs. In the recovery stress process, some ε-martensite transforms back to γ-austenite, while additional dislocations and new ε-martensite variants with different orientations relationship. The schematic summarizes the complex interactions between dislocations, TBs, and reversible/irreversible martensitic transformation that influence the PE and shape memory behavior.

5. Summary

This study investigates the influence of thermo-mechanical processing on the functional properties of an Fe–17Mn–5Si–10Cr–4Ni-1 (V–C) (wt.%) shape memory alloy. The as-received material was subjected to cold rolling followed by recrystallization and aging treatments. The microstructure, phase fractions, PE, SME, and recovery stress were studied. The key findings are summarized as follows:

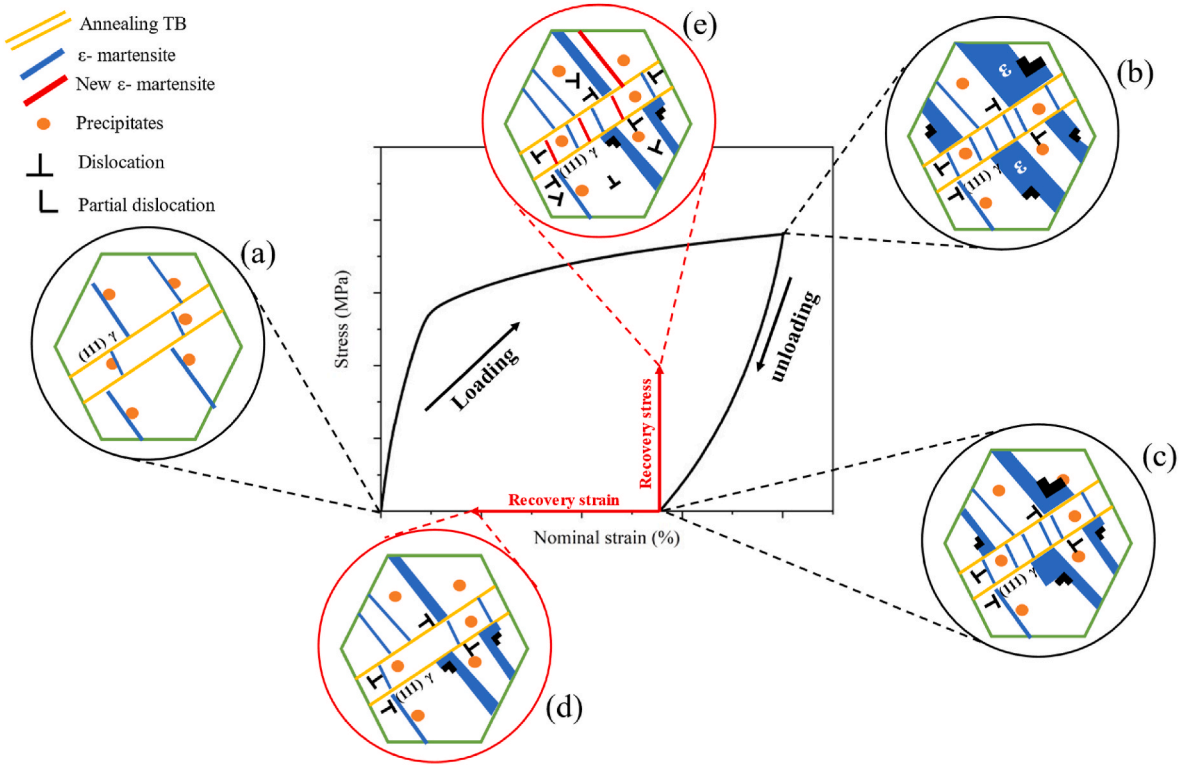

Fig. 12. Schematic representation of the microstructural evolution in FeMnSi shape memory alloys (SMAs) during different processing steps: (a) Initial state of the Rex-double aged sample; (b) Microstructure at the peak loading point; (c) after unloading. Comparing the microstructural changes during (d) the recovery strain test and (e) the recovery stress test.

- Cold rolling and recrystallization refined the grain size from 14 to 5 μm and introduced a high density of annealing twins. The second aging treatment at 485 °C further increased the density of nano-sized VC precipitates.
- Cyclic tensile testing showed an improved pseudoelasticity in the recrystallized and double aged condition, with minimal cumulative residual strain over 50 cycles. This was attributed to the strong precipitation strengthening and interactions between martensite and the refined microstructural features.
- The recrystallized and double aged specimen displayed the highest recovery stress of 450 MPa upon heating after pre-straining. This was attributed to the highest ε-martensite phase fraction after the load-unload test and the high yield strength suppressing new martensite formation during the cooling process.
- HR-TEM revealed a non-Shoji-Nishiyama orientation relationship between the new ε-martensite which forms after the recovery stress formation and austenite matrix, which differs from conventional loading conditions. This contributes to an additional irrecoverable strain and increases the recovery stress.

In summary, optimization of the thermo-mechanical processing parameters can enable tailoring the functional properties of FeMnSi shape memory alloys according to the desired applications. The recrystallization and double aging treatment can produce an alloy with excellent cyclic stability and the highest recovery stress.

Declaration of competing interest

The authors declare that they have no known competing financial interests or personal relationships that could have appeared to influence the work reported in this paper.

Acknowledgment

The authors gratefully acknowledge the support from re-fer AG, Switzerland, for providing the material used in this research study. Financial support from the Iran National Science Foundation (INSF) through research grant No. 4015297 is also acknowledged by M.N.A.

Appendix A

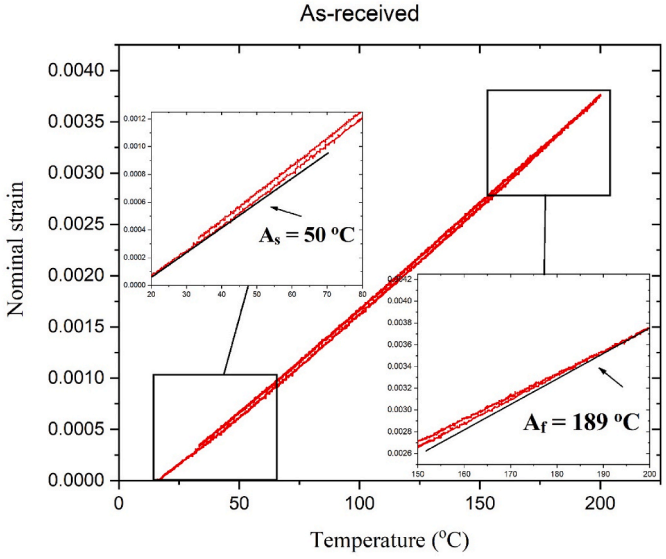

Fig. 1. Thermal Analysis of Dilatometry: Heatingp and Cooling Process at 2 °C/min for As-received Sample, with A_s and A_f Determined from the Curve.

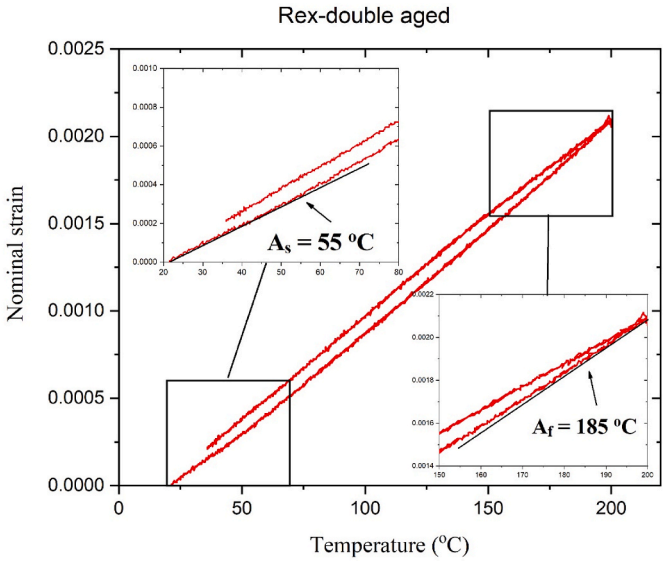

Fig. 2. Thermal Analysis of Dilatometry: Heating and Cooling Process at 2 °C/min for Rex-double aged Sample, with A_s and A_f Determined from the Curve.

References

[1] Otsuka K, Wayman CM. Shape memory materials. New York: Cambridge Univ, Press; 1998.

[2] Gu XL, Chen ZY, Yu QQ, Ghafoori E. Stress recovery behavior of an Fe-Mn-Si shape memory alloy. Eng Struct 2021;243:112710. https://doi.org/10.1016/J.ENGSTRUCT.2021.112710.

[3] Janke L, Czaderski C, Motavalli M, Ruth J. Applications of shape memory alloys in civil engineering structures—overview. limits and new ideas, Materials and Structures 2005;38:578–92. https://doi.org/10.1007/BF02479550. 5 38 (2005).

[4] Leinenbach C, Kramer H, Bernhard C, Eifler D. Thermo-mechanical properties of an Fe–Mn–Si–Cr–Ni–VC shape memory alloy with low transformation temperature. Adv Eng Mater 2012;14:62–7. https://doi.org/10.1002/ADEM.201100129.

[5] Leinenbach C, Lee WJ, Lis A, Arabi-Hashemi A, Cayron C, Weber B. Creep and stress relaxation of a FeMnSi-based shape memory alloy at low temperatures. Mater Sci Eng, A 2016;677:106–15. https://doi.org/10.1016/J.MSEA.2016.09.042.

[6] Koohdar HR, Nili-Ahmadabadi M, Habibi-Parsa M, Jafarian HR, Ghasemi-Nanesa H, Shirazi H. Observation of pseudoelasticity in a cold rolled Fe–Ni–Mn martensitic steel. Mater Sci Eng, A 2016;658:86–90. https://doi.org/10.1016/J.MSEA.2016.01.113.

[7] Sato A, Chishima E, Soma K, Mori T. Shape memory effect in γ⇄ϵ transformation in Fe-30Mn-1Si alloy single crystals. Acta Metall 1982;30:1177–83. https://doi.org/10.1016/0001-6160(82)90011-6.

[8] Sato A, Chishima E, Yamaji Y, Mori T. Orientation and composition dependencies of shape memory effect IN Fe-Mn-Si alloys. Acta Metall 1984;32:539–47. https://doi.org/10.1016/0001-6160(84)90065-8.

[9] Kajiwara S, Kikuchi T. Shape memory effect and related transformation behavior in Fe□Ni□C alloys. Acta Metall Mater 1990;38:847–55. https://doi.org/10.1016/0956-7151(90)90038-I.

[10] Tseng LW, Ma J, Wang SJ, Karaman I, Kaya M, Luo ZP, Chumlyakov YI. Superelastic response of a single crystalline FeMnAlNi shape memory alloy under tension and compression. Acta Mater 2015;89:374–83. https://doi.org/10.1016/J.ACTAMAT.2015.01.009.

[11] Sehitoglu H, Karaman I, Zhang XY, Chumlyakov Y, Maier HJ. Deformation of FeNiCoTi shape memory single crystals. Scripta Mater 2001;44:779–84. https://doi.org/10.1016/S1359-6462(00)00657-6.

[12] Sawaguchi T, Kikuchi T, Kajiwara S. The pseudoelastic behavior of Fe–Mn–Si-based shape memory alloys containing Nb and C. Smart Mater Struct 2005;14:S317. https://doi.org/10.1088/0964-1726/14/5/022.

[13] Sawaguchi T, Maruyama T, Otsuka H, Kushibe A, Inoue Y, Tsuzaki K. Design concept and applications of Fe–Mn–Si-based alloys—from shape-memory to seismic response control. Mater Trans 2016;57:283–93. https://doi.org/10.2320/MATERTRANS.MB201510.

[14] Sawaguchi T, Tomota Y, Yoshinaka F, Harjo S. Evidence supporting reversible martensitic transformation under cyclic loading on Fe–Mn–Si–Al alloys using in situ neutron diffraction. Acta Mater 2023;242:118494. https://doi.org/10.1016/J.ACTAMAT.2022.118494.

[15] Koster M, Lee WJ, Schwarzenberger M, Leinenbach C. Cyclic deformation and structural fatigue behavior of an FE–Mn–Si shape memory alloy. Mater Sci Eng, A 2015;637:29–39. https://doi.org/10.1016/J.MSEA.2015.04.028.

[16] Ghafoori E, Hosseini E, Leinenbach C, Michels J, Motavalli M. Fatigue behavior of a Fe-Mn-Si shape memory alloy used for prestressed strengthening. Mater Des 2017;133:349–62. https://doi.org/10.1016/J.MATDES.2017.07.055.

[17] Hosseini E, Ghafoori E, Leinenbach C, Motavalli M, Holdsworth SR. Stress recovery and cyclic behaviour of an Fe–Mn–Si shape memory alloy after multiple thermal activation. Smart Mater Struct 2018;27:025009. https://doi.org/10.1088/1361-665X/AAA2C9.

[18] Lee WJ, Weber B, Feltrin G, Czaderski C, Motavalli M, Leinenbach C. Phase transformation behavior under uniaxial deformation of an Fe–Mn–Si–Cr–Ni–VC shape memory alloy. Mater Sci Eng, A 2013;581:1–7. https://doi.org/10.1016/J.MSEA.2013.06.002.

[19] Murakami M, Yamada H, Maruyama T, Tanahashi H. Effects of alloying additions on Fe-Mn-Si shape memory alloys. ISIJ Int 1990;30:674–9. https://doi.org/10.2355/ISIJINTERNATIONAL.30.674.

[20] Lee TH, Shin E, Oh CS, Ha HY, Kim SJ. Correlation between stacking fault energy and deformation microstructure in high-interstitial-alloyed austenitic steels. Acta Mater 2010;58:3173–86. https://doi.org/10.1016/J.ACTAMAT.2010.01.056.

[21] Liu D, Kajiwara S, Kikuchi T, Shinya N, Wang D, Liu W. Mechanism of the improvement of the shape memory effect by "training" and ausforming in Fe–Mn–Si based shape memory alloys. Mater Trans, JIM 2000;41:593–6. https://doi.org/10.2320/MATERTRANS1989.41.593.

[22] Ogawa K, Kajiwara S. HREM study of stress-induced transformation structures in an Fe–Mn–Si–Cr–Ni shape memory alloy. Mater Trans, JIM 1993;34:1169–76. https://doi.org/10.2320/MATERTRANS1989.34.1169.

[23] Zambrano OA, Logé RE. Dynamic recrystallization study of a Fe-Mn-Si based shape memory alloy in constant and variable thermomechanical conditions. Mater Char 2019;152:151–61. https://doi.org/10.1016/J.MATCHAR.2019.04.016.

[24] Kim YS, Choi E, Kim WJ. Characterization of the microstructures and the shape memory properties of the Fe-Mn-Si-Cr-Ni-C shape memory alloy after severe plastic deformation by differential speed rolling and subsequent annealing. Mater Char 2018;136:12–9. https://doi.org/10.1016/J.MATCHAR.2017.11.055.

[25] Wen YH, Peng HB, Raabe D, Gutierrez-Urrutia I, Chen J, Du YY. Large recovery strain in Fe-Mn-Si-based shape memory steels obtained by engineering annealing twin boundaries. Nat Commun 2014;5:1–9. https://doi.org/10.1038/ncomms5964. 1 5 (2014).

[26] Kajiwara S, Liu D, Kikuchi T, Shinya N. Remarkable improvement of shape memory effect in Fe-Mn-Si based shape memory alloys by producing NbC precipitates. Scripta Mater 2001;44:2809–14. https://doi.org/10.1016/S1359-6462(01)00978-2.

[27] Farjami S, Hiraga K, Kubo H. Shape memory effect and crystallographic investigation in VN containing Fe-Mn-Si-Cr alloys. Mater Trans 2004;45:930–5. https://doi.org/10.2320/MATERTRANS.45.930.

[28] Wei Z, Yuhua W, Ning L, Wenling X, Shanhua W. Directional precipitation of carbides induced by γ/ε interfaces in an FeMnSiCrNiC alloy aged after deformation at different temperature. Mater Sci Eng, A 2007;459:324–9. https://doi.org/10.1016/J.MSEA.2007.01.005.

[29] Lai MJ, Li YJ, Lillpopp L, Ponge D, Will S, Raabe D. On the origin of the improvement of shape memory effect by precipitating VC in Fe–Mn–Si-based shape memory alloys. Acta Mater 2018;155:222–35. https://doi.org/10.1016/J.ACTAMAT.2018.06.008.

[30] Shahverdi M, Michels J, Czaderski C, Motavalli M. Iron-based shape memory alloy strips for strengthening RC members: material behavior and characterization.

Construct Build Mater 2018;173:586–99. https://doi.org/10.1016/J.CONBUILDMAT.2018.04.057.
[31] Wen YH, Li N, Xiong LR. Composition design principles for Fe–Mn–Si–Cr–Ni based alloys with better shape memory effect and higher recovery stress. Mater Sci Eng, A 2005;407:31–5. https://doi.org/10.1016/J.MSEA.2005.08.054.
[32] Baruj A, Kikuchi T, Kajiwara S, Shinya N. Effect of pre-deformation of austenite on shape memory properties in Fe-Mn-Si-based alloys containing Nb and C. Mater Trans 2002;43:585–8. https://doi.org/10.2320/MATERTRANS.43.585.
[33] Wang CP, Wen YH, Peng HB, Xu DQ, Li N. Factors affecting recovery stress in Fe–Mn–Si–Cr–Ni–C shape memory alloys. Mater Sci Eng, A 2011;528:1125–30. https://doi.org/10.1016/J.MSEA.2010.10.068.
[34] Yang Y, Arabi-Hashemi A, Leinenbach C, Shahverdi M. Influence of thermal treatment conditions on recovery stress formation in an FeMnSi-SMA. Mater Sci Eng, A 2021;802:140694. https://doi.org/10.1016/J.MSEA.2020.140694.
[35] Emani SV, Benedyk J, Nash P, Chen D. Double aging and thermomechanical heat treatment of AA7075 aluminum alloy extrusions. J Mater Sci 2009;44:6384–91. https://doi.org/10.1007/S10853-009-3879-8/FIGURES/15.
[36] Epicier T, Acevedo D, Perez M. Crystallographic structure of vanadium carbide precipitates in a model Fe-C-V steel. Phil Mag 2008;88:31–45. https://doi.org/10.1080/14786430701753816.
[37] Yang Y, Leinenbach C, Shahverdi M. Simulation and experimental characterization of VC precipitation and recovery stress formation in an FeMnSi-based shape memory alloy. J Alloys Compd 2023;940:168856. https://doi.org/10.1016/J.JALLCOM.2023.168856.
[38] Khodaverdi H, Mohri M, Ghafoori E, Ghorabaei AS, Nili-Ahmadabadi M. Enhanced pseudoelasticity of an Fe-Mn-Si-based shape memory alloy by applying microstructural engineering through recrystallization and precipitation. J Mater Res Technol 2022;21:2999–3013. https://doi.org/10.1016/j.jmrt.2022.10.092.
[39] Khodaverdi H, Mohri M, Ghorabaei AS, Ghafoori E, Nili-Ahmadabadi M. Effect of low-temperature precipitates on microstructure and pseudoelasticity of an Fe–Mn–Si-based shape memory alloy. Mater Char 2023;195. https://doi.org/10.1016/j.matchar.2022.112486.
[40] Mohri M, Ferretto I, Khodaverdi H, Leinenbach C, Ghafoori E. Influence of thermomechanical treatment on the shape memory effect and pseudoelasticity behavior of conventional and additive manufactured Fe-Mn-Si-Cr-Ni-(V,C) shape memory alloys. J Mater Res Technol 2023. https://doi.org/10.1016/J.JMRT.2023.04.195.
[41] Mohri M, Ferretto I, Leinenbach C, Kim D, Lignos DG, Ghafoori E. Effect of thermomechanical treatment and microstructure on pseudo-elastic behavior of Fe–Mn–Si–Cr–Ni-(V, C) shape memory alloy. Mater Sci Eng, A 2022;855:143917. https://doi.org/10.1016/J.MSEA.2022.143917.
[42] Jafarabadi A, Ferretto I, Mohri M, Leinenbach C, Ghafoori E. 4D printing of recoverable buckling-induced architected iron-based shape memory alloys. Mater Des 2023:112216. https://doi.org/10.1016/J.MATDES.2023.112216.
[43] Felice IO, Shen J, Barragan AFC, Moura IAB, Li B, Wang B, Khodaverdi H, Mohri M, Schell N, Ghafoori E, Santos TG, Oliveira JP. Wire and arc additive manufacturing of Fe-based shape memory alloys: microstructure, mechanical and functional behavior. Mater Des 2023;231:112004. https://doi.org/10.1016/J.MATDES.2023.112004.
[44] Mohri M, Ferretto I, Khodaverdi H, Leinenbach C, Ghafoori E. Influence of thermomechanical treatment on the shape memory effect and pseudoelasticity behavior of conventional and additive manufactured Fe–Mn–Si–Cr–Ni-(V,C) shape memory alloys. J Mater Res Technol 2023;24:5922–33. https://doi.org/10.1016/J.JMRT.2023.04.195.
[45] Leinenbach C, Arabi-Hashemi A, Lee WJ, Lis A, Sadegh-Ahmadi M, Van Petegem S, Panzner T, Van Swygenhoven H. Characterization of the deformation and phase transformation behavior of VC-free and VC-containing FeMnSi-based shape memory alloys by in situ neutron diffraction. Mater Sci Eng, A 2017;703:314–23. https://doi.org/10.1016/J.MSEA.2017.07.077.
[46] Zhang C, Yu Q, Tang YT, Xu M, Wang H, Zhu C, Ell J, Zhao S, MacDonald BE, Cao P, Schoenung JM, Vecchio KS, Reed RC, Ritchie RO, Lavernia EJ. Strong and ductile FeNiCoAl-based high-entropy alloys for cryogenic to elevated temperature multifunctional applications. Acta Mater 2023;242:118449. https://doi.org/10.1016/J.ACTAMAT.2022.118449.
[47] Mohri M, Ferretto I, Leinenbach C, Kim D, Lignos DG, Ghafoori E. Effect of thermomechanical treatment and microstructure on pseudo-elastic behavior of Fe–Mn–Si–Cr–Ni-(V, C) shape memory alloy. Mater Sci Eng, A 2022;855:143917. https://doi.org/10.1016/J.MSEA.2022.143917.
[48] Stanford N, Dunne DP. Effect of second-phase particles on shape memory in Fe–Mn–Si-based alloys. Mater Sci Eng, A 2007;454–455:407–15. https://doi.org/10.1016/J.MSEA.2006.11.084.
[49] Stanford N, Dunne DP. Effect of NbC and TiC precipitation on shape memory in an iron-based alloy. J Mater Sci 2006;41:4883–91. https://doi.org/10.1007/S10853-006-0050-7/FIGURES/11.
[50] Yang Y, Arabi-Hashemi A, Leinenbach C, Shahverdi M. Influence of thermal treatment conditions on recovery stress formation in an FeMnSi-SMA. Mater Sci Eng, A 2021;802:140694. https://doi.org/10.1016/J.MSEA.2020.140694.
[51] Group PM, Division M. Martensiti c transformatio n zenji nishiyama. 1972. p. 480.
[52] Jee KK, Jang WY, Chung YH. Preferred orientation of rolling-induced $\varepsilon $ martensite in an Fe-Mn-Si alloy. J Phys IV 2003;112:365–8. https://doi.org/10.1051/JP4:2003902.
[53] Robertson JH. IUCr, elements of X-ray diffraction by B. D. Cullity, urn:issn:0567-7394 35. 1979. https://doi.org/10.1107/S0567739479000917. 350–350.
[54] De Cooman BC, Estrin Y, Kim SK. Twinning-induced plasticity (TWIP) steels. Acta Mater 2018;142:283–362. https://doi.org/10.1016/J.ACTAMAT.2017.06.046.
[55] Remy L. Kinetics of f.c.c. deformation twinning and its relationship to stress-strain behaviour. Acta Metall 1978;26:443–51. https://doi.org/10.1016/0001-6160(78)90170-0.
[56] Hung CY, Bai Y, Shimokawa T, Tsuji N, Murayama M. A correlation between grain boundary character and deformation twin nucleation mechanism in coarse-grained high-Mn austenitic steel. Sci Rep 2021;11:1–13. https://doi.org/10.1038/s41598-021-87811-w. 1 11 (2021).
[57] Dong Z, Klotz UE, Leinenbach C, Bergamini A, Czaderski C, Motavalli M. A novel Fe-Mn-Si shape memory alloy with improved shape recovery properties by VC precipitation. Adv Eng Mater 2009;11:40–4. https://doi.org/10.1002/ADEM.200800312.
[58] Stanford N, Dunne DP, Li H. Re-examination of the effect of NbC precipitation on shape memory in Fe–Mn–Si-based alloys. Scripta Mater 2008;58:583–6. https://doi.org/10.1016/J.SCRIPTAMAT.2007.11.018.
[59] Peng H, Wang G, Wang S, Chen J, MacLaren I, Wen Y. Key criterion for achieving giant recovery strains in polycrystalline Fe-Mn-Si based shape memory alloys. Mater Sci Eng, A 2018;712:37–49. https://doi.org/10.1016/J.MSEA.2017.11.071.
[60] Stanford NE, Chen K, Dunne DP, Jin XJ. Effect of alloying additions on the SFE, neél temperature and shape memory effect in Fe–Mn–Si-based alloys. ISIJ Int 2007;47:883–9. https://doi.org/10.2355/ISIJINTERNATIONAL.47.883.
[61] Li Q, Cahoon JR, Richards NL. Effects of thermo-mechanical processing parameters on the special boundary configurations of commercially pure nickel. Mater Sci Eng, A 2009;527:263–71. https://doi.org/10.1016/J.MSEA.2009.07.064.
[62] Luo Q, Wen H, Bu D, Peng H, Wen Y. Correlation between shape memory effect and density of annealing twin boundary in an FeMnSiCrNi alloy during special heat treatments with different parameters. Mater Sci Eng, A 2022;859:144213. https://doi.org/10.1016/J.MSEA.2022.144213.
[63] Kajiwara S. Characteristic features of shape memory effect and related transformation behavior in Fe-based alloys. Mater Sci Eng, A 1999;273–275:67–88. https://doi.org/10.1016/S0921-5093(99)00290-7.
[64] Orowan E. Fracture and strength of solids. Rep Prog Phys 1949;12:185. https://doi.org/10.1088/0034-4885/12/1/309.
[65] Daitoh Y, Torizuka S, Hanamura T. Mechanism of strengthening by vanadium carbide precipitation in pearlite in microalloyed steels. Tetsu-To-Hagane/Journal of the Iron and Steel Institute of Japan 2011;97:480–5. https://doi.org/10.2355/TETSUTOHAGANE.97.480.
[66] Il Baik S, Kim YW. A transmission electron microscopy study of strain-induced secondary twin and epsilon-martensitic transformation in Fe-15Mn-2Cr-0.6C-0.06N austenitic steel. Materialia (Oxf) 2020;10:100677. https://doi.org/10.1016/J.MTLA.2020.100677.